

Application of Novel Filtering Approaches to Modern Space Domain Awareness

Jonathan Kadan *, **Dylan Thomas** *, **Amit Bala** *
Virginia Polytechnic Institute and State University
Kevin Schroeder, PhD †, **Jonathan Black, PhD** ‡
Virginia Polytechnic Institute and State University

ABSTRACT

To keep up with the demands of current and future Space Domain Awareness (SDA), a fast and accurate estimator is necessary. The Adapted Structural (AST) Unscented Kalman Filter (UKF) has been shown to provide more Gaussian results compared to the Earth Centered Inertial (ECI) UKF and Equinoctial (EQ) UKF. The AST-UKF will be evaluated against an space object catalog with satellites in all orbital regimes with a distributed Space Surveillance Network to see if it is a viable candidate for the future of SDA.

1. INTRODUCTION

A well-known issue in Space Domain Awareness (SDA) is that orbit propagation of an Earth Centered Inertial (ECI) state is inherently non-linear. Standard Kalman Filters (KF) and Extended Kalman Filters (EKF) do not approximate nonlinear state transition matrices well which leads to numerical errors [8]. The Unscented Kalman Filter (UKF) overcomes this problem in SDA as it can handle the nonlinear dynamics of Resident Space Objects (RSO) orbit propagation by creating 13 sigma points with the unscented transformation [11]. However, this statistical approximation of estimate covariances are less Gaussian than a more accurate estimator, such as the particle filtering technique would produce.

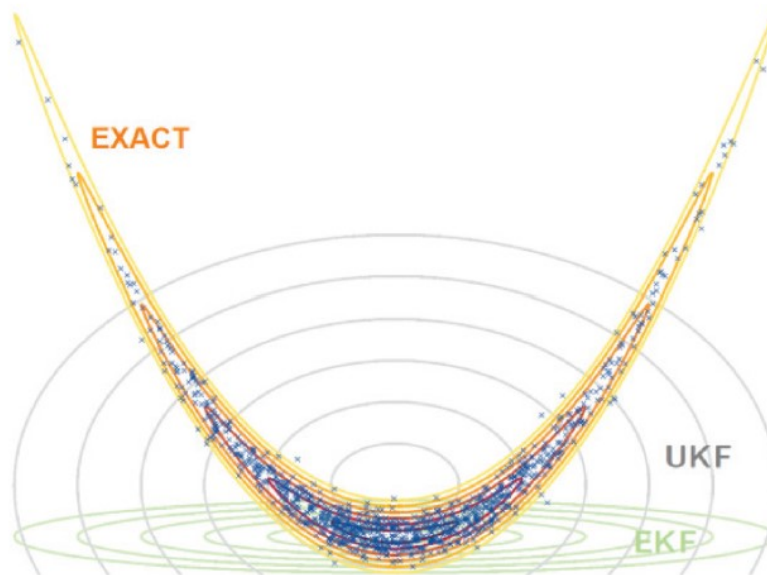


Fig. 1: Propagated Distribution Comparison of Orbital States [1]

*Graduate Research Assistant, Kevin T. Crofton Department of Aerospace and Ocean Engineering

†Research Scientist, Hume Center for National Security and Technology

‡Professor, Kevin T. Crofton Department of Aerospace and Ocean Engineering

The non-Gaussian nature of Earth centered inertial (ECI) estimate covariances stretch much further in the in-track direction compared to cross-track and radial directions (RIC coordinates). As can be seen in Figure 1, the center of the UKF Gaussian is, on average, at a slightly lower orbit than the true center of the RSO being estimated. In orbital dynamics, this means that the estimate will be at a lower altitude than it should be and therefore have less energy. Over this time, the error compounds itself leading to degrading orbital radius and estimate divergence. Left untreated long enough, especially in LEO orbits, estimates with this compounding error may have sigma points on re-entry orbits.

There are multiple ways to overcome this issue, such as decreasing time step and lowering filter noise magnitude. The difference in standard deviation for different filter noise magnitudes can be seen in Table 1. However, these techniques diminish the advantage of using the UKF, which is its lower computational cost compared to the particle filtering technique. With the future of SDA having to account for the massive increase in RSO in the coming years due to upcoming proliferated LEO (p-LEO) constellations, e.g. Starlink, the need for quickly resolved tasking solutions and accurate estimates has never been higher [6]. If the UKF was applied to a linear coordinate system, the results would be Gaussian and therefore closer to the correct altitude.

Table 1: ECI position and velocity standard deviation growth from un-modeled dynamics

Filter noise magnitude	Position std (m)	Velocity std (mm/s)
$1e-7$	948.6	5477.2
$1e-10$	30.0	173.2
$1e-15$	0.094	0.547
Unmodeled	$\delta_r = 1/2at^2 \simeq 0.045\text{m}$	$\delta_v = at \simeq 0.3\text{mm/s}$

Luckily, such a technique already exists, as the ‘‘Adapted STructural’’ Unscented Kalman Filter (AST-UKF) was developed for this very purpose [5]. The AST coordinate system is a derivation of the equinoctial coordinate system and is more Gaussian compared to standard ECI coordinates [5]. This is because the AST coordinate system is derived in such a way that all RSO have an initial inclination of 0 degrees in their relative orbital frame. This results in no issue with retrograde orbits with an inclination of 180 degrees, a known problem in propagating in the equinoctial frame [10]. While this orbit type is rare, the ability to account for this edge case would give an advantage to the AST-UKF compared to the equinoctial UKF (EQ-UKF).

This work compares the AST-UKF and EQ-UKF to the standard ECI-UKF on a scale necessary for modern SDA. In particular this paper focuses on the affects of high fidelity special perturbations dynamics models on these Kalman filters and evaluates their performance and stability through the use of catalog statistics and pair plot analysis. This work generated and studied 24-hour scenarios with dozens of RSO across multiple orbital regimes (LEO, MEO and GEO) and a representative Space Surveillance Network (SSN) based on open source information that incorporates optical (2D), radar (3D) and advanced radar (4D) observations. The specifications for the sensor locations and capabilities simulated can be found in [2] and the orbital regimes and distributions of RSO used in this work is shown in Table 2.

Table 2: Target Set Distribution

Orbital Regime	Number of Targets	Percentage of set
LEO	52	75.36%
MEO	5	7.24%
GEO	12	17.39%

A sub-optimal partially observed Markov decision process (POMDP) will be implemented to autonomously task this diverse, distributed sensor network to track a potentially maneuvering, non-uniform RSO. For this work, the reward function used in the POMDP Number 14 from Appendix B of [2]. This tool has the capability to simulate weeks of sensor tasking solutions for hundreds of RSO and will be used as the simulator for evaluating the ECI-UKF and AST-UKF algorithms. Multiple evaluation metrics were used including: root mean square (RMS) estimate position error, Mahalanobis distance, and observation count [2].

This work expands upon the previous AST studies by combining 2D, 3D, and 4D observations into the AST-UKF

filtering solution for the first time [4]. The value in this research is the potential foundation for rapid SDA based on large scale simulation of a more accurate estimation algorithm across multiple orbital regimes.

2. AST COORDINATES

To mitigate the issues of nonlinearity in dynamics, the breakdown of Gaussian assumptions, and energy loss, Adaptive Structural (AST) coordinates are implemented. AST coordinates are designed such that uncertainty in the state can be represented using Gaussian distributions [3].

AST Coordinates, as defined in [3, 4] are a modified version of equinoctial coordinates using the central radial-tangential-normal (CRTN) reference basis. AST solutions were derived from the starting point of an initial state given in ECI coordinates, and are transformed to ECI using the rotation matrix described in Equation 1.

$$R^{(c)} = [\mathbf{u}^{\text{CRTN}} \mathbf{v}^{\text{CRTN}} \mathbf{w}^{\text{CRTN}}] \quad (1)$$

where \mathbf{u}^{CRTN} , \mathbf{v}^{CRTN} , and \mathbf{w}^{CRTN} denote the RTN basis for the central state, CRTN. Also note that \mathbf{u}^{CRTN} , \mathbf{v}^{CRTN} , and \mathbf{w}^{CRTN} are each [3x1] vectors, creating a [3x3] $R^{(c)}$ rotation matrix. From the rotation matrix defined in equation 1, the state vectors for the central states can be defined in equation 2.

$$\mathbf{x}^{(\text{CRTN})}(t) = R^{(c)T} \mathbf{x}^{\text{ECI}(c)}(t), \dot{\mathbf{x}}^{(\text{CRTN})}(t) = R^{(c)T} \dot{\mathbf{x}}^{\text{ECI}(c)}(t) \quad (2)$$

where $\mathbf{x}^{\text{ECI}(c)}(t)$ and $\dot{\mathbf{x}}^{\text{ECI}(c)}(t)$ represent the ECI position and ECI velocity at time t , respectively. The [6x1] CRTN-ECI state vector can be generate by stacking $\mathbf{x}^{(c)}(t)$ and $\dot{\mathbf{x}}^{(c)}(t)$. From the [6x1] state vector now given with respect to the CRTN frame, the classical orbital elements (COE) were calculated, as prescribed in equation 6 of [10]. In the transformation from CRTN-ECI to COE, be careful when calculating eccentric anomaly, it is recommended to use tangent inverse shown in the top left of equation 6, while accounting for quadrant checks with some version of atan2 (MATLAB) or numpy.arctan2 (Python) depending on the programming language used and angle normalization $[0, 2\pi)$.

From the derived orbital elements, the 6 AST coordinates can be defined, as shown in equation 3

$$A_1 = 2 \tan(i/2) \cos(\Omega), A_2 = 2 \tan(i/2) \sin(\Omega), A_3(t) = \phi(t), A_4 = e \cos(\theta_p), A_5 = e \sin(\theta_p), A_6 = n \quad (3)$$

where the angles θ_p , ϕ_p , and ϕ_t are defined in equations 4, 5, and 7:

$$\theta_p = \Omega + \omega \quad (4)$$

Ω and ω represent the right ascension of the ascending node (RAAN) and argument of periapsis, respectively.

$$\phi_p = F_{T-t_0-M}(\theta_p, e) \quad (5)$$

and $F_{T-t_0-M}(\theta_p, e)$ is defined as the transformation from True Anomaly to Mean Anomaly, with the variable θ_p substituted for the true anomaly T . The detailed version of $F_{T-t_0-M}(\theta_p, e)$ can be seen here, calculated from a modified version of eccentric anomaly (E) in terms of θ_p :

$$\phi_p = E - e \sin(E), E = 2 \operatorname{atan} \left(\sqrt{\frac{1-e}{1+e}} \tan \left(\frac{\theta_p}{2} \right) \right) \quad (6)$$

This transformation is derived from equations in [9]. Finally, $\phi(t)$ can be calculated via:

$$\phi(t) = \phi_p + M(t) \quad (7)$$

where $M(t)$ is defined as the mean anomaly of the orbit at time t .

Initially, equation 3 is used to transform the definition of the initial state from the ECI frame to AST reference coordinates. During the propagation process states are transformed back from AST coordinates into the ECI system, and

following propagation, back into AST coordinates. First, the AST coordinates are used to derive the classical orbital elements eccentricity, direction of perigee with respect to the CRTN preferred reference direction, inclination, RAAN, argument of perigee, semi-major, and true anomaly with respect to time in the CRTN basis, as shown in equations 8-14:

$$e = \sqrt{A_4^2 + A_5^2} \quad (8) \quad \omega = \theta_p - \Omega \quad (12)$$

$$\theta_p = \text{atan2}(A_5, A_4) \quad (9) \quad a = \mu^{1/3} / A_6^{2/3} \quad (13)$$

$$i = 2\text{atan}(A_2, A_3) \quad (10)$$

$$\Omega = \text{atan2}(A_2, A_1) \quad (11) \quad T(t) = A_3(t) - \theta_p \quad (14)$$

From the results of these equations, the data is then transformed back into ECI coordinates using the solution provided in [9].

3. MODIFICATIONS TO ECI-UKF

At the initialization of each scenario, a necessary value is saved to each estimate RSO object that will be called upon later. For the EQ-UKF, that value is f_r , a scalar denoting whether or not an orbit is in retrograde motion [10]. In the AST-UKF, the CRTN is saved, because it never changes with time and is necessary for all transformation to and from AST coordinates [4].

Inside the UKF itself, the first modification is in the predict step. A detailed representation of the algorithm used for the UKF predictions can be found in Algorithm 2.3 of [8]. Between steps 3 and 4 of Algorithm 2.3, each AST coordinate sigma point is converted to ECI coordinates. Using equations 8 - 14 in section 3, the Keplerian elements in the CRTN frame are generated. Next, these COE's are transformed into the CRTN-ECI frame using equation 5 from [10]. Finally, the CRTN-ECI state is converted into standard ECI coordinates using the transpose of $R^{(c)}$ as shown:

$$\mathbf{x}^{\text{ECI}}(t) = R^{(c)} \mathbf{x}^{(\text{CRTN})}(t), \dot{\mathbf{x}}^{\text{ECI}(c)}(t) = R^{(c)} \dot{\mathbf{x}}^{(\text{CRTN})}(t) \quad (15)$$

Now in standard ECI coordinates, the sigma points are propagated through the special perturbations dynamics module (which will be described in greater detail in the next section). After propagation, each new ECI state vector is transformed into AST coordinates through the processes described in section 2.

In the UKF forecast step, detailed in Algorithm 2.4 in [8], each predicted sigma point is converted to ECI so that observation predictions can be. Because this conversion, it is possible to forecast more than angles-only observations. These observation predictions are saved in the South East Zenith (SEZ) frame and evaluated for possible sensor tasking by the simulation's POMDP.

4. SPECIAL PERTURBATIONS

To model RSO at the highest fidelity possible, a dynamics model that includes special perturbation components. While these components may only minutely vary an RSO state vector, they can significantly alter scenarios simulated for multiple days at large time steps. Shown in Table 3 are the special perturbation components used in this work, compared to the default settings in Analytical Graphics, Inc.'s (AGI) System Tool Kit (STK) HPOPv10 propagator.

It is important to model many different perturbations because they affect certain orbital regimes more than others. The major difference between the two special perturbation models is the lack of a drag model in Virginia Tech's simulation environment.

Table 3: Special Perturbation Comparison

Perturbation	STK	VT
Drag	Jaccia-Roberts	N/A
SRP	Spherical	Spherical
3rd Body	Sun, Moon	Sun, Moon
EGM	4x4 EGM2008	4x4 EGM96

In this development, three different perturbation models were considered and modeled: the 4x4 Earth Gravity Model (EGM), solar radiation pressure (SRP), and 3rd body sun and moon perturbations. A 4x4 Earth Gravity Model, and in particular 4x4 EGM96 was considered in this work to model Earth's non-spherical and zonal harmonics effects. The dashed blue line in Figure 2 represents level of special perturbation fidelity used in this work. Constants corresponding to the 4th-degree and 4th-order model were taken from [7].

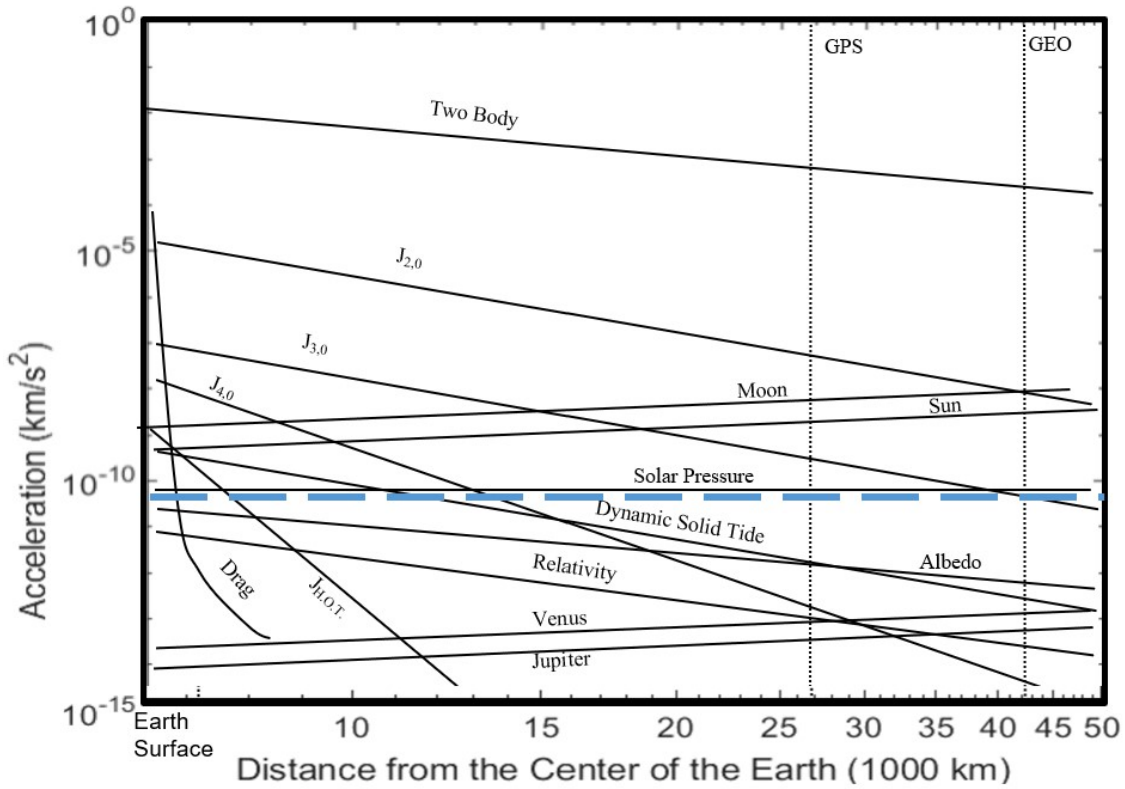


Fig. 2: Order of magnitude of special perturbations for satellite orbits [7].

As described in [7], satellites exposed to solar radiation are subjected to a small force that is caused by the absorption and reflection of photons. The force exerted on a satellite due to solar radiation pressure is defined in equation 16.

$$F = -P_{\odot} \cos(\theta)A[(1 - \varepsilon)\mathbf{e}_{\odot} + 2\varepsilon \cos(\theta)\mathbf{n}] \quad (16)$$

where $-P_{\odot}$ represents the solar radiation pressure, A is the area of the surface coming into contact with the solar radiation, ε is the reflectivity of the surface, \mathbf{e}_{\odot} is the eccentricity vector of the heliocentric orbit, and \mathbf{n} is the direction vector normal to A .

As also described in [9], satellites in an Earth-centered reference frame may be subjected to acceleration forces due to

a third body, such as the sun or moon. The acceleration due to a third body is defined in equation 17

$$\vec{a}_3 = \vec{r}_{sat3} Q - \frac{\vec{r}_{sat3}}{r_{\oplus 3}^3} \quad (17)$$

where \vec{r}_{sat3} is the direction vector from the satellite to the third body, $r_{\oplus 3}^3$ is the magnitude of the direction vector from the second to the third body, and Q is defined in equation 18:

$$Q = \frac{(r_{\oplus sat}^2 + 2(\vec{r}_{\oplus sat} \cdot \vec{r}_{sat3})) (r_{\oplus 3}^2 + r_{\oplus 3} r_{sat3} + r_{sat3}^2)}{r_{\oplus 3}^3 r_{sat3}^3 (\vec{r}_{\oplus 3} + \vec{r}_{sat3})} \quad (18)$$

with $\vec{r}_{\oplus sat}$ representing the direction vector between the satellite and second central body, \vec{r}_{sat3} representing the direction vector between the satellite and the third body.

5. RESULTS

5.1 Pair Plots

To assess the utility of AST coordinates compared to standard equinoctial coordinates, two cases were created to demonstrate behaviors at separate uncertainty magnitudes. Case 1 covers a “nominal” uncertainty realization of $\sigma = 1.5\text{km}$ in each position coordinate and $\tau = 0.002\text{km/s}$ in each velocity coordinate. Meanwhile, Case 2 scales up to higher uncertainties of $\sigma = 15\text{km}$ and $\tau = 0.02\text{km/s}$, respectively. The pair plots were generated by sampling 200 points around a mean ECI state which was selected as one of the MEO catalog targets simulated for Section 5.2. Then, the ECI points were propagated forward 12 hours, after which they were then transformed into the requisite coordinates to show how the point cloud shifted over time.

5.1.1 Case 1: Nominal uncertainty in position and velocity

In Figures 3 and 4, the pair plots of AST and equinoctial coordinates are shown for the nominal uncertainty case. The diagonals are histograms of the corresponding coordinate’s and give insight to the overall variance. The off-diagonals show the covariances between across different combinations of coordinates. These pair plots are given to demonstrate, qualitatively, how the two coordinates preserve the initial Gaussian distribution after propagation.

In examining Figure 3, it becomes clear that the AST coordinates do not provide a significant advantage over standard equinoctial coordinates for this test case. Both pair plots appear to remain visually Gaussian across all dimensions. Also, both coordinate sets include two dimensions that are highly coordinated (three and six for AST, one and six for equinoctial). Finally, the histograms of each coordinate set appear to loosely follow Gaussian behavior. The corresponding pair plots for ECI and COE coordinates are given by Figure 7 in Appendix 6.

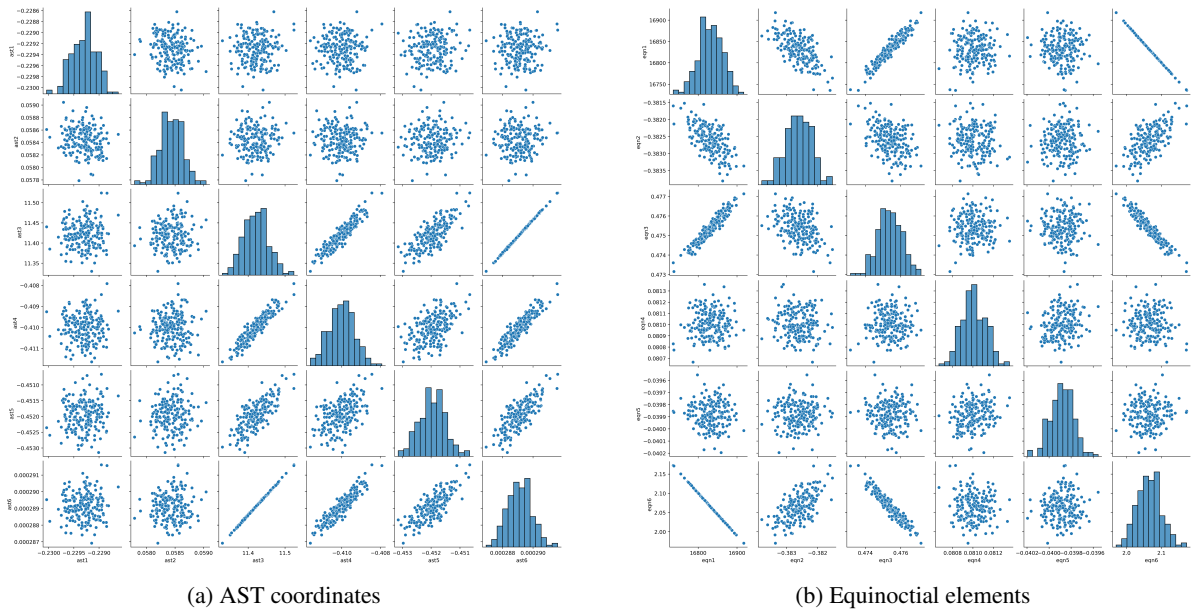


Fig. 3: Pairs plots of AST and equinoctial coordinates with nominal uncertainty

5.1.2 Case 2: High uncertainty in position and velocity

In Case 2, the uncertainty was increased by an order of magnitude in both position and velocity. Figure 3 shows the pair plots of propagate points in both AST and equinoctial coordinates. Again, the histograms of all dimensions in both coordinates appear to approximate a Gaussian distribution. The covariances across dimensions have remained well-approximated by Gaussian behavior as well. The main change from the nominal case to the current case is that a few of the dimensions have become more correlated. The only appreciable difference between AST and equinoctial coordinates in this case is that more AST covariances have remained “spread” or uncorrelated. In contrast, more equinoctial covariance plots are beginning to show strong correlations. The corresponding pair plots for ECI and COE coordinates are given by Figure 8 in Appendix 6.

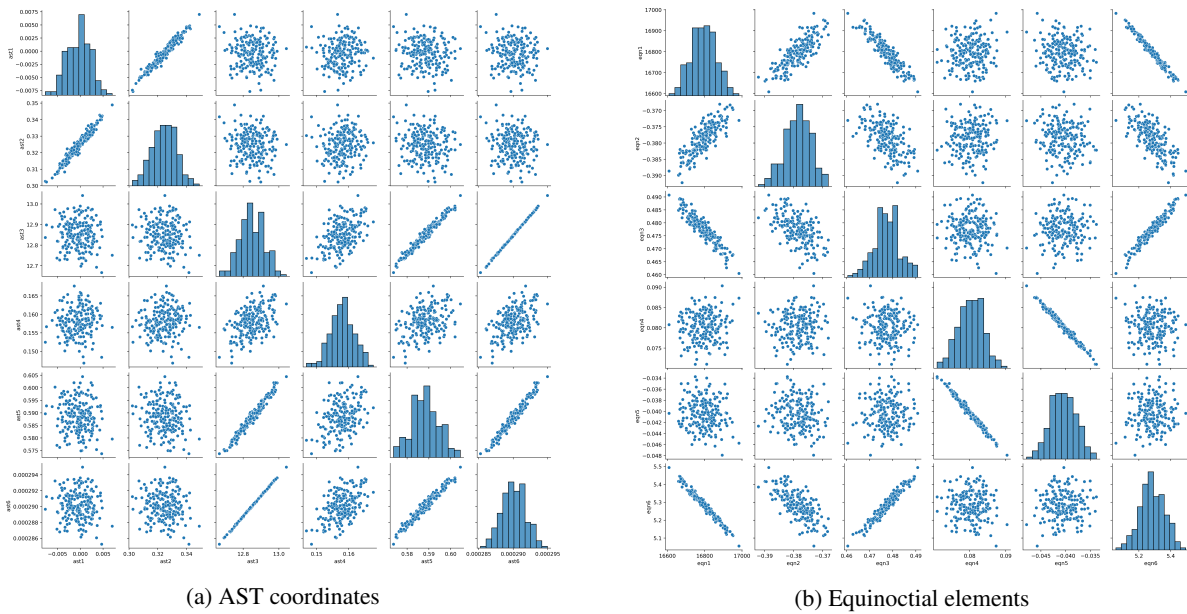


Fig. 4: Pairs plots of AST and equinoctial coordinates with high uncertainty

5.2 Estimate Error and Catalog Statistics

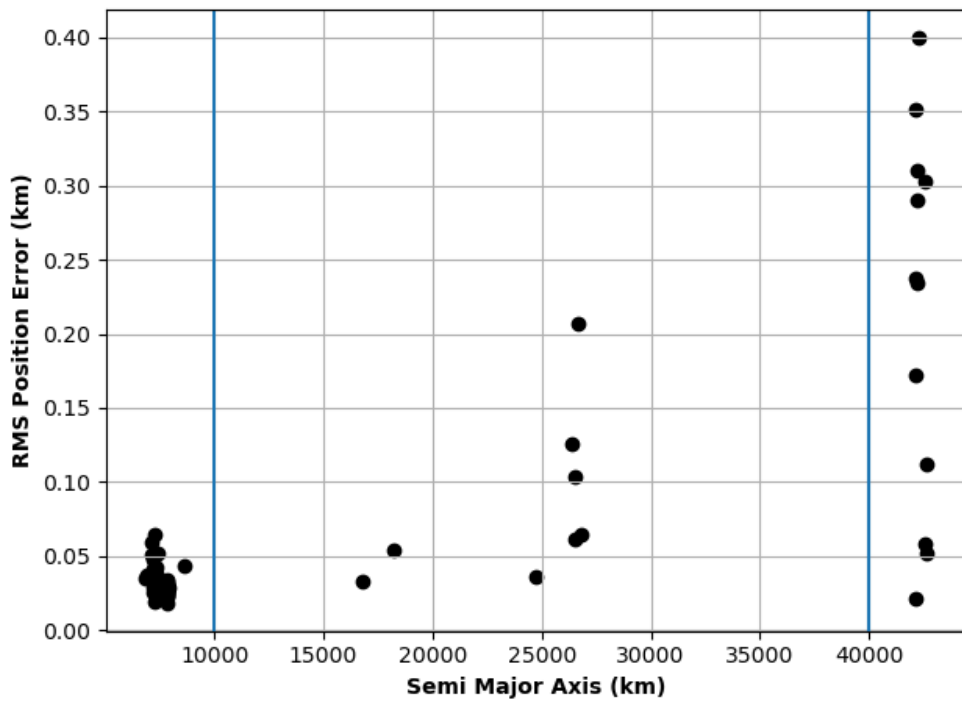


Fig. 5: Scenario ECI RMS position error plotted against RSO semimajor axis

As can be seen in Figure 5, the RMS position error is extremely small, and grows with semimajor axis, which is to be expected because observation quality decreases with distance. However, the estimate position error may be extremely small for a LEO RSO, as a drag model was not considered in the special perturbations dynamics in this simulation.

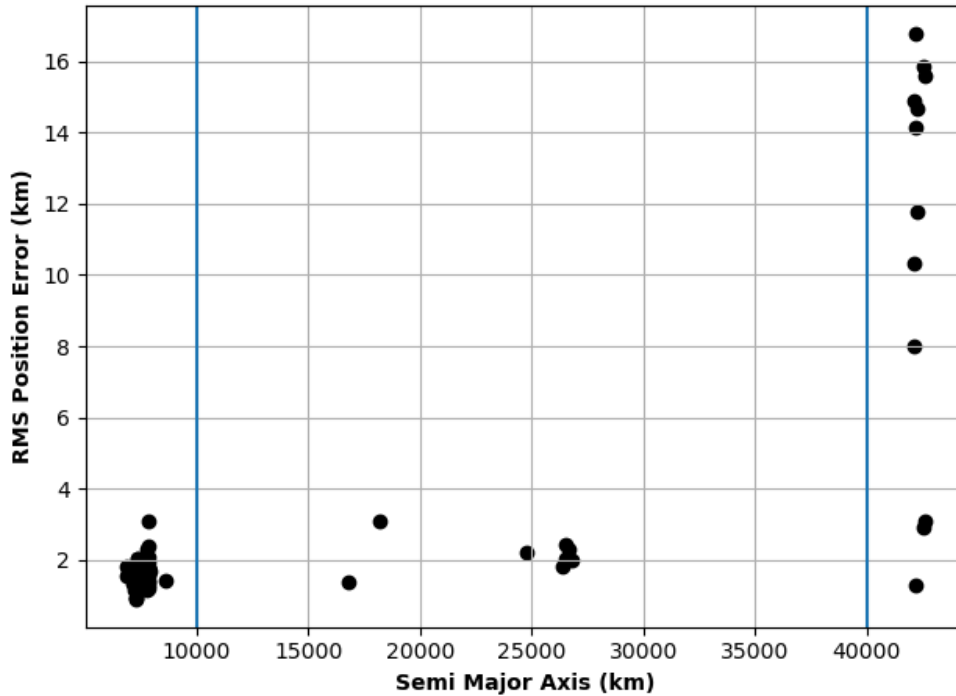


Fig. 6: Scenario EQ RMS position error plotted against RSO semimajor axis

The results from the equinoctial filter follow a similar trend as the ECI results, but at a high overall magnitude. Again, the lack of drag-modeling may artificially decrease the estimate position error in LEO. At this time-step level, the added stability of the EQ-UKF does not outperform possible numerical error induced by coordinate transformations.

Table 4: Catalog Statistics Results

Coord. System	RMS position error (km)	Mahalanobis distance (km)	Lost RSO	Observations per RSO
ECI	0.1208	0.7291	0	100.5
EQ	5.67777	621.72	9	109.6

Unfortunately, it was not possible to generate estimate error statistics for the AST-UKF. It is hypothesized that the linearization techniques used to develop this coordinate system caused numerical issues inside the AST-UKF and lead to estimate state divergence.

6. CONCLUSIONS

When comparing the uncertainty propagation of a point cloud in AST coordinates versus equinoctial coordinates, both appeared to hold the Gaussian assumption across relevant use cases. The variances and covariances of neither coordinate's pair plots showed strong evidence of skewness or multi-modality. Because of this, these show promise as coordinates in which error covariances should be well behaved.

The AST-UKF was unable to maintain the stability needed propagate inside a high fidelity orbital dynamics model. This was most likely caused by the linearization needed to instantiate an AST coordinate system in the CRTN frame. The EQ-UKF produced results adequate for SDA, but the need to perform special perturbations calculations in ECI and to transform coordinates have increased the estimate error by an order of magnitude.

Looking towards potential future efforts, it would be beneficial to run scenarios with larger time steps (all the work

presented here consisted of 5 minute timesteps) to see if ECI estimate error degrades quicker compared to EQ and AST. Also, while the target set used contained RSO from all orbital regimes, a larger and more diverse target set would give a more complete picture. More work is needed to properly characterize the statistics of AST coordinates when used directly in a UKF. Follow on studies will perform Monte Carlo simulations to try and cover a more complete set of cases by which we can measure the effectiveness of AST coordinates. In particular, it would be helpful to determine (and fully explore) the edge cases in which AST coordinates are well-suited and equinoctial are not.

APPENDIX A: EXAMPLE TRANSFORMATION

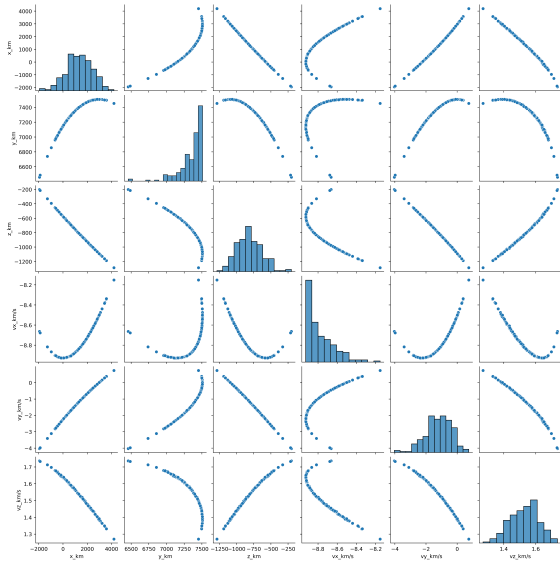
Following the precedent and initial orbit provided in [10], the converted states to the CRTN basis, classical orbital elements, and AST coordinates in the CRTN basis, based upon the equations in the Solution section of this paper, are provided for reference: The 6x1 initial ECI orbit state of a LEO RSO in a polar orbit as given in [10] is provided, along with the 6x1 state in the CRTN Basis, and the 6x1 state in AST Coordinates:

6x1 Orbital States		
ECI State	CRTN Basis State	AST State
-605.79922166	6.85769636e+03	0.00000
-5870.2295111	9.09494702e-13	0.00000
3493.0531990	-1.13686838e-13	6.10622664e-14
-1.568254290	7.36281286e-03	4.46072075e-04
-3.702348910	7.62564535	-9.65963780e-04
-6.479483950	-2.22044605e-16	1.11099025e-03

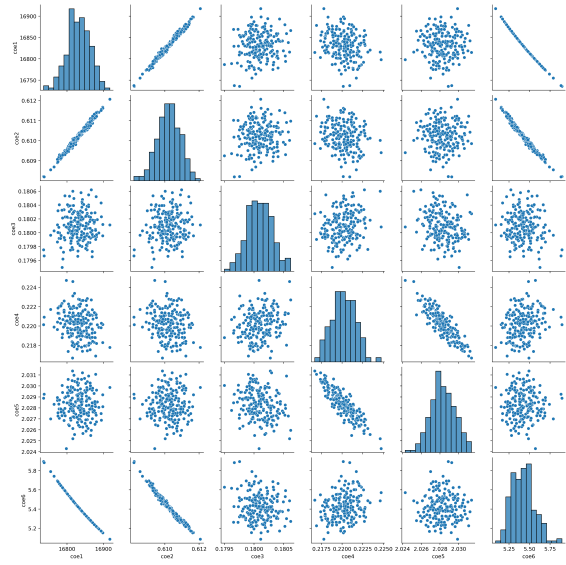
The following table provides key classical orbital elements used in equations 3, 4, 5, and 7, as well as the orbital elements that are subsequently calculated from the AST state in equations 8, 9, 10, 11, 12, and 13.

Orbital Elements Before and After AST Transformations		
Orbital Element	Original State	After AST Transformation
Semi-major axis (km)	6860.7631	6860.763154253214
Inclination (deg)	97.65184	N/A
Eccentricity	0.0010610	0.0010639860530936122
Right Ascension (deg)	79.54701	N/A
Argument of Periapsis (deg)	83.86041	N/A
True Anomaly (rad)	1.1381820887	1.1381814942281174

APPENDIX B: ADDITIONAL PAIR PLOTS

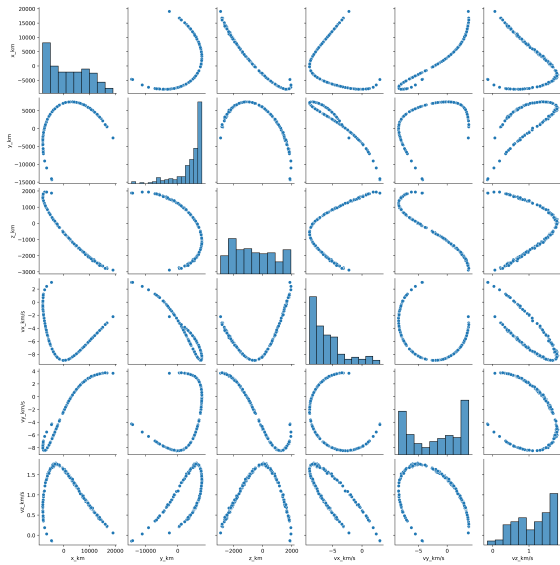


(a) ECI coordinates

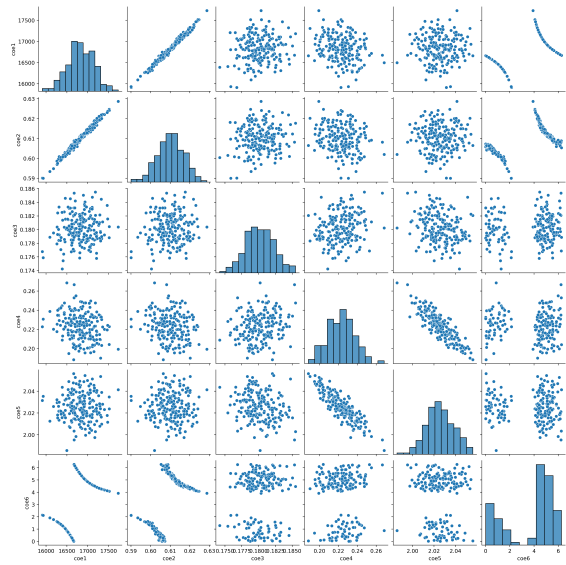


(b) Classical elements

Fig. 7: Pairs plots of ECI (a) and COE (a) coordinates with nominal uncertainty



(a) ECI coordinates



(b) Classical elements

Fig. 8: Pairs plots of ECI (a) and COE (b) coordinates with high uncertainty

REFERENCES

- [1] National Research Council et al. *Continuing Kepler's Quest: Assessing Air Force Space Command's Astrodynamics Standards*. National Academies Press, 2012.
- [2] et al. Kadan, Jonathan. Parametric analysis of an autonomous sensor tasking engine for spacecraft tracking. *AIAA Scitech 2021 Forum*, 2021.
- [3] John T Kent, Shambo Bhattacharjee, Weston R Faber, and Islam I Hussein. Revisiting the orbital tracking problem. *arXiv preprint arXiv:1909.03793*, 2019.
- [4] John T Kent, Shambo Bhattacharjee, Weston R Faber, and Islam I Hussein. A unified approach to the orbital tracking problem. In *2020 IEEE International Conference on Multisensor Fusion and Integration for Intelligent Systems (MFI)*, pages 82–87. IEEE, 2020.
- [5] John T Kent, Shambo Bhattacharjee, Islam I Hussein, and Moriba Jah. Nonlinear filtering using directional statistics for the orbital tracking problem with perturbation effects. In *2018 Space Flight Mechanics Meeting*, page 0474, 2018.
- [6] Jonathan C. McDowell. The low earth orbit satellite population and impacts of the SpaceX starlink constellation. *The Astrophysical Journal*, 892(2):L36, apr 2020.
- [7] Oliver Montenbruck, Eberhard Gill, and Fh Lutze. Satellite orbits: models, methods, and applications. *Appl. Mech. Rev.*, 55(2):B27–B28, 2002.
- [8] Kevin Michael Nastasi. *Autonomous and Responsive Surveillance Network Management for Adaptive Space Situational Awareness*. PhD thesis, Virginia Tech, 2018.
- [9] David A Vallado. *Fundamentals of astrodynamics and applications*, volume 12. Springer Science & Business Media, 2001.
- [10] David A Vallado and Salvatore Alfano. Updated analytical partials for covariance transformations and optimization. In *Proceedings of the 2015 AAS/AIAA Astrodynamics Specialist Conference*, 2015.
- [11] Eric A Wan, Rudolph Van Der Merwe, and Simon Haykin. The unscented kalman filter. *Kalman filtering and neural networks*, 5(2007):221–280, 2001.